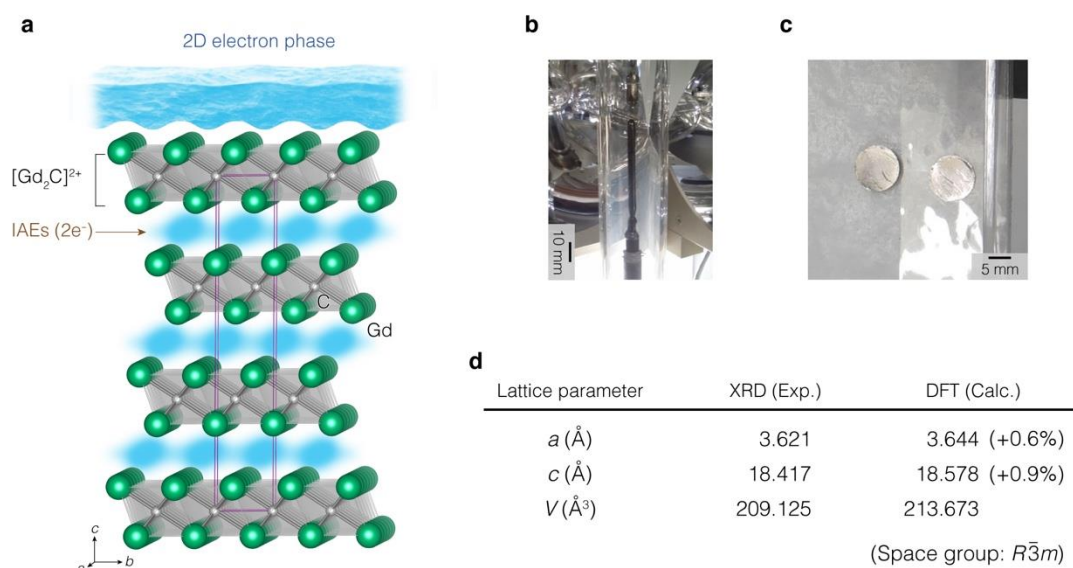
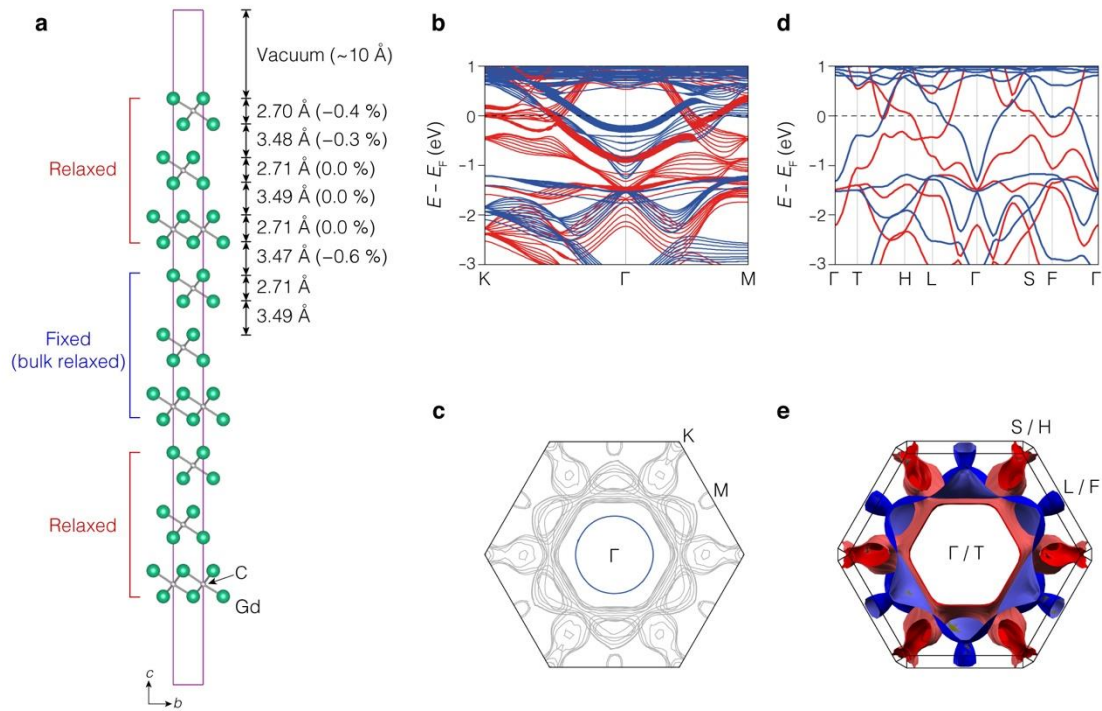


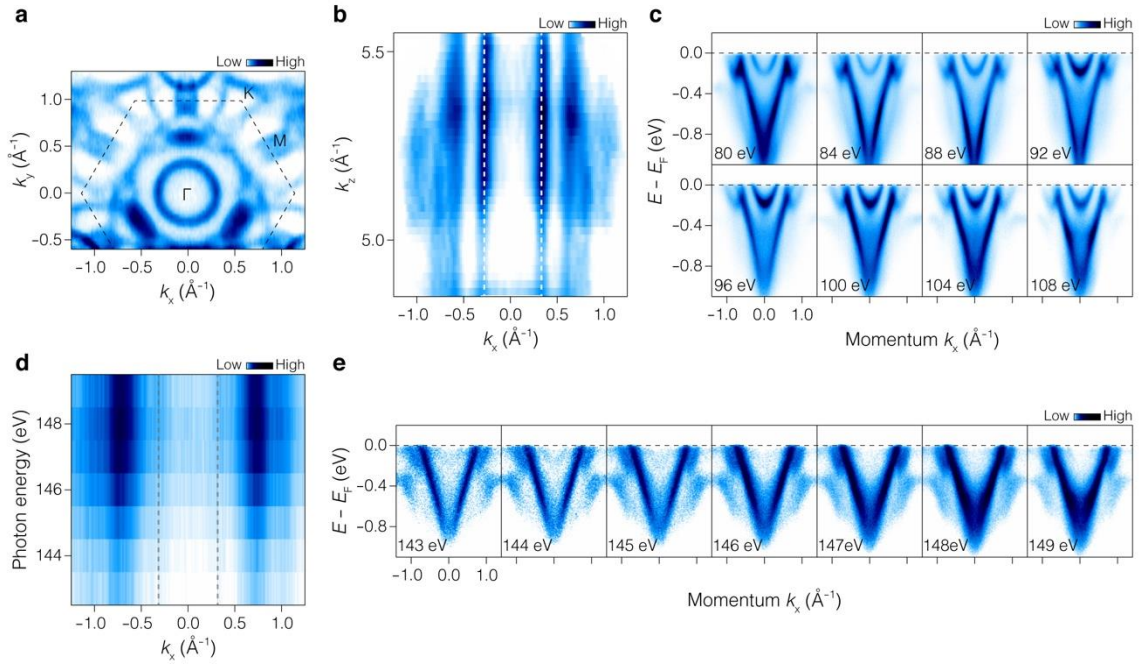
## Extended data figures and tables



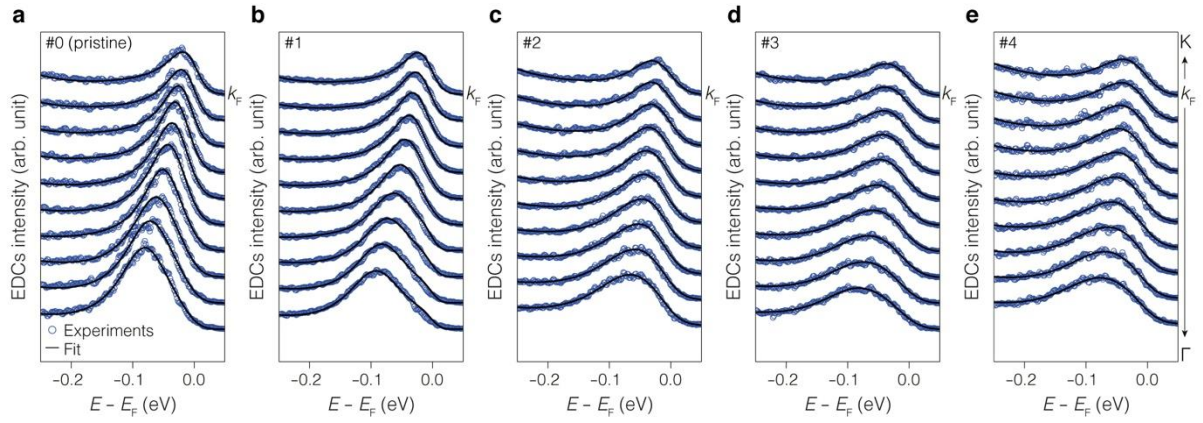
**Extended Data Figure 1 | Crystal structure of the 2D  $[\text{Gd}_2\text{C}]^{2+}\cdot 2\text{e}^-$  electride.** **a**, Anti- $\text{CdCl}_2$ -type layered structure of  $[\text{Gd}_2\text{C}]^{2+}\cdot 2\text{e}^-$  with a space group of  $R\bar{3}m$ . The cationic slab  $[\text{Gd}_2\text{C}]^{2+}$  is composed of an edge-sharing octahedra structure and is separated by the interlayer space. IAEs (brown arrow) are confined between the positively charged  $[\text{Gd}_2\text{C}]^{2+}$  layers. The 2D electrons distinct from IAEs are floated on the topmost  $[\text{Gd}_2\text{C}]^{2+}$  layer. The purple lines indicate the unit cell. **b,c**, Photographs of single crystal  $[\text{Gd}_2\text{C}]^{2+}\cdot 2\text{e}^-$  rod with 50 mm length grown by floating zone melting method (**b**) and as-cleaved crystal by 3M Scotch tape (**c**). **d**, Lattice parameters obtained by the XRD measurements<sup>21</sup> and the DFT calculations.



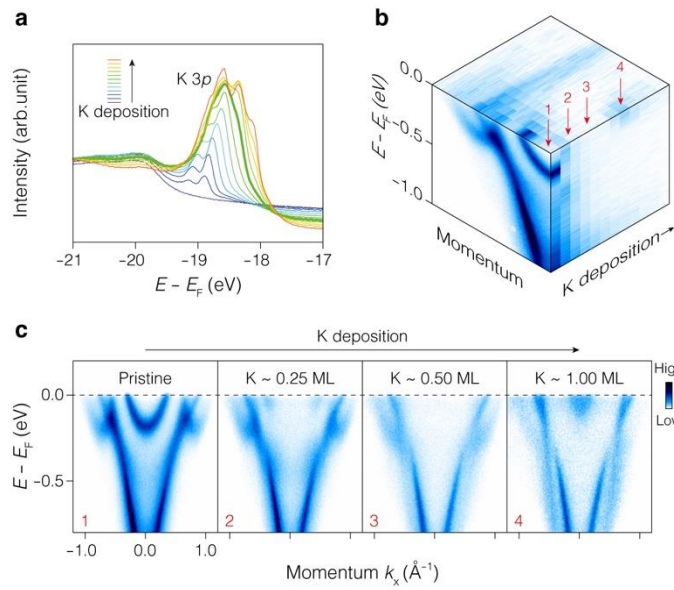
**Extended Data Figure 2 | The detailed electronic structure of  $[\text{Gd}_2\text{C}]^{2+}\cdot 2\text{e}^-$  obtained by DFT calculations.** **a**, Relaxed crystal structure of the nine-slab model for the slab calculations.  $a \times b \times 3c$  supercell with a vacuum of  $20 \text{ \AA}$  along the  $c$ -axis was used. For the relaxation of the nine-slab model, the optimised bulk structure was used for the central three-layer, while the three layers at both ends of the slab were relaxed. **b,c**, Calculated band structure and the Fermi surface of  $[\text{Gd}_2\text{C}]^{2+}\cdot 2\text{e}^-$  using the nine-slab model, respectively. Blue and red colours indicate spin up and spin down components, respectively. Band thickness represents the contribution of the surface electrons. The thicker line has a contribution mainly from the surface character. **d,e**, Band structure and the Fermi surface (top view along  $k_z$  direction) of  $[\text{Gd}_2\text{C}]^{2+}\cdot 2\text{e}^-$  obtained by bulk calculation, respectively. In contrast to the result from the nine-slab model, the bulk calculation does not reproduce the parabolic band dispersion with cylindrical 2D Fermi surface observed by ARPES (Fig. 2a and Extended Data Fig. 3a–c).



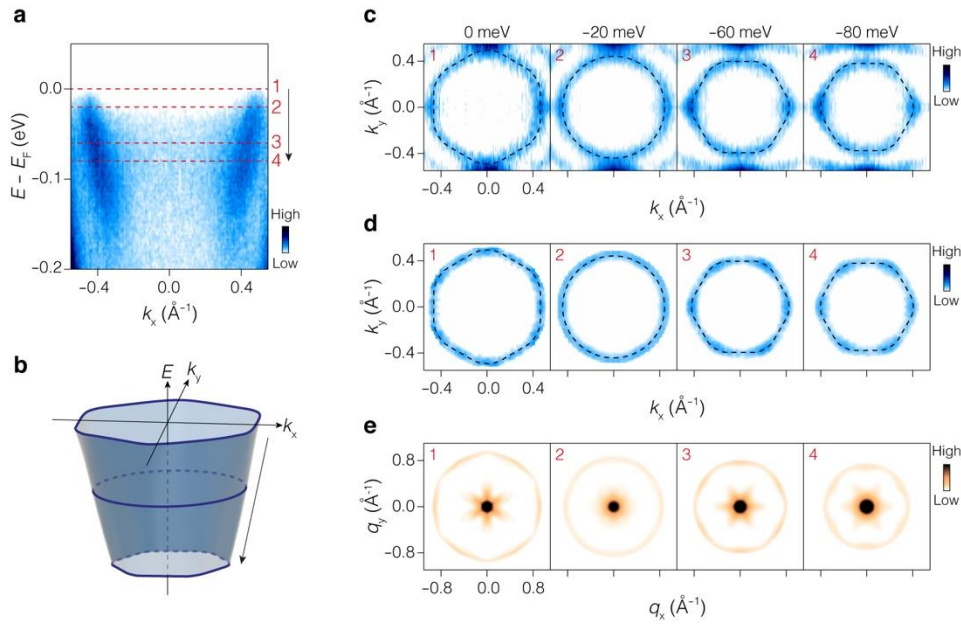
**Extended Data Figure 3 | Fermi surface of surface electrons on  $[\text{Gd}_2\text{C}]^{2+}\cdot 2\text{e}^-$  and photon energy dependence.** **a**, In-plane ( $k_x$ - $k_y$ ) Fermi surface of  $[\text{Gd}_2\text{C}]^{2+}\cdot 2\text{e}^-$ . The black dashed line indicates the BZ. Circular Fermi surface near BZ centre corresponds to the parabolic band dispersion exhibited in Fig. 2a. **b**, Fermi surface in the  $k_x$ - $k_z$  plane. The inner straight surface, overlaid by dashed white lines, is from the parabolic band shown in Fig. 2a and from the circular Fermi surface in **a**. **c**, Band dispersion observed at various photon energies from 80 to 108 eV with every 4 eV step to obtain  $k_x$ - $k_z$  plane Fermi surface in **b**. **d**, Photon energy-dependent ARPES intensity map extracted from the Fermi level taken with photon energies from 143 to 149 eV, which includes both on- and off-resonant conditions of Gd 4d core level. Dashed grey lines are overlaid on the surface 2D electron band as a guide for the eye. The IAE band intensity at 148 eV greatly increased, a clear resonance behaviour while changing in the intensity of the surface 2D electron band is far weak through the whole photon energies. **e**, Detailed band dispersions at each photon energy in **d** are exhibited.



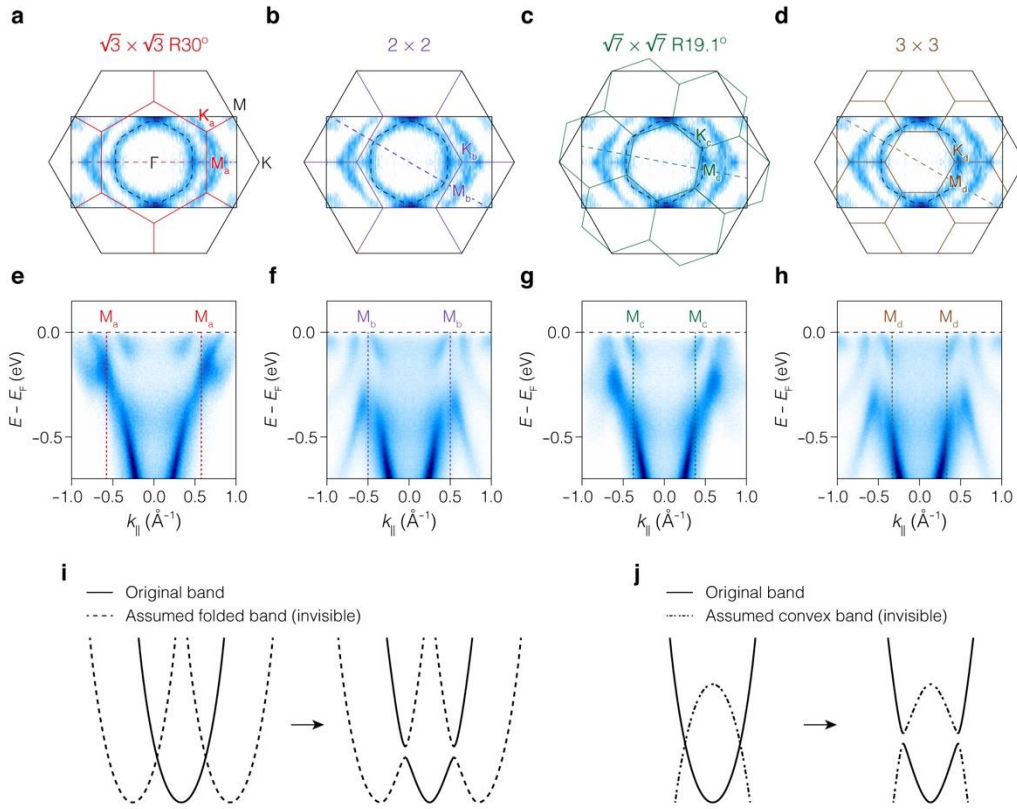
**Extended Data Figure 4 | Line shape analysis. a–e**, EDCs (blue) taken near Fermi momenta ( $k_F$ ) along  $\Gamma$ –K direction for different deposition steps #0–#4 in Fig. 4, respectively. To extract the scattering rate shown in Figs. 3c and 4d, EDCs are fitted with a fitting curve generated by multiplication of the Lorentzian curves convoluted with the Gaussian curve for accounting the experimental resolution. Solid black curves represent the result of the fitting. Plotted scattering rates, corresponding to the imaginary part of self-energy, in Figs. 3c and 4d are obtained from the half width at half maximum of the Lorentzian curve for the surface electron band.



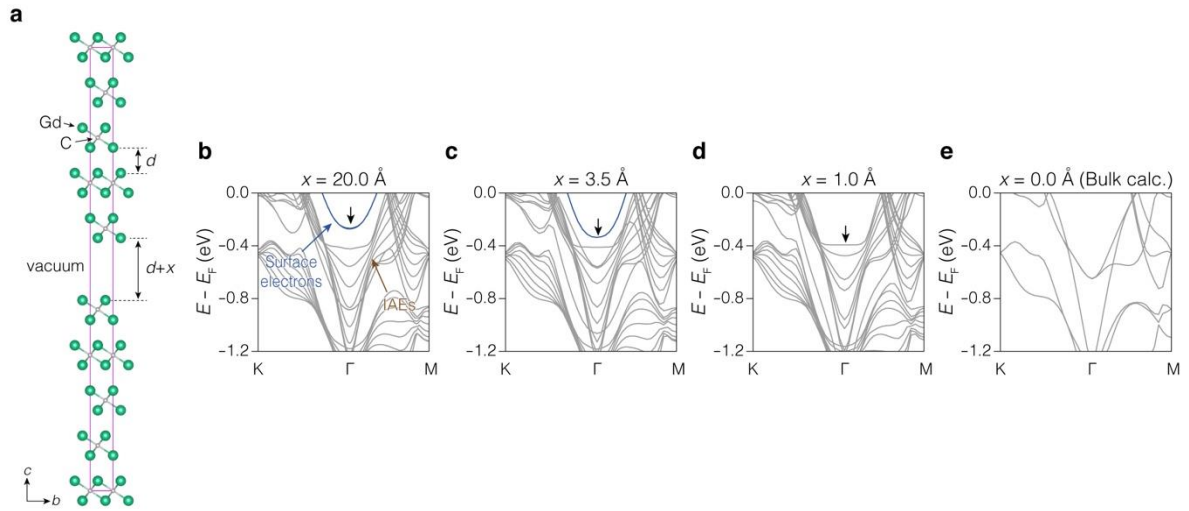
**Extended Data Figure 5 | Determination of K coverage.** **a**, Core-level spectra of K 3p with different K coverage on the cleaved  $[\text{Gd}_2\text{C}]^{2+} \cdot 2\text{e}^-$  surface. The K 3p core-level peak starts to grow with K deposition near the binding energy of 19 eV and eventually saturates where we estimate the coverage as 1 ML (thick green curve). Above 1 ML, chemically shifted additional peaks emerge at lower binding energy close to 18 eV. **b**, A 3D representation of the band evolution with increasing K coverage. **c**, Extracted band dispersion at several different K coverages indicated by red arrows in **b**. Surface 2D electron band (1) evolves via K deposition (2) and disappears (3). This implies the surface electron density is actually reduced by K deposition. In the rightmost panel (4), corresponding to K 1 ML, which we estimate with core-level spectra in **a**, K band appears near Fermi level, which well agrees with the core level estimation.



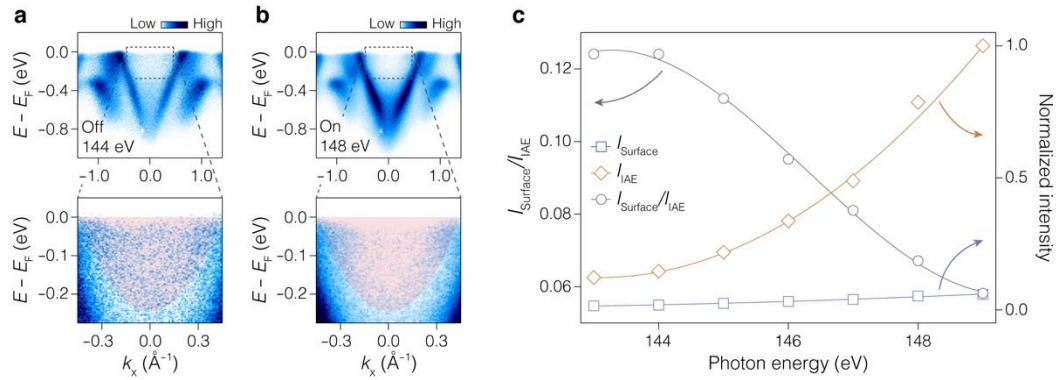
**Extended Data Figure 6 | Analysis for the hexagonal topology.** **a**, Focused band dispersion of 0.25 ML K coverage, corresponding to deposition step #6 in Fig. 4a. **b**, Schematic band structure of the ARPES result in **a**. Blue solid lines schematically show constant energy contours (CECs) at different energies. **c**, CECs obtained at binding energies of 0, 20, 60, and 80 meV, indicated with dashed red lines (1–4) in **a**. **d**, Symmetrized CECs with 3-fold rotation after removing the intensity from the outer band in **c**, which reveals the shape of energy contours from the quantum electrons more clearly. Overlaid dashed black lines in **c** and **d** are guides for the topology of each CEC. The guidelines evidence that the original shape of contours is not deformed by 3-fold symmetrisation. **e**, Autocorrelation analyses performed with CECs of corresponding energies in **d**, which clearly visualise the angular dependence of the band along with the in-plane momentum.



**Extended Data Figure 7 | Scenarios of W-shape band deformation.** **a-d**, Fermi surface with 0.25 ML K coverage. BZs of several possible surface superstructures with sub-ML coverage of K,  $\sqrt{3} \times \sqrt{3} R30^\circ$  (**a**),  $2 \times 2$  (**b**),  $\sqrt{7} \times \sqrt{7} R19.1^\circ$  (**c**), and  $3 \times 3$  (**d**), respectively, are overlaid with a different colour. The outermost hexagon with solid black line represents the BZ of  $1 \times 1$  unit cell of  $[\text{Gd}_2\text{C}]^{2+} \cdot 2\text{e}^-$ . **e-h**, Observed band dispersion along the  $\Gamma$ - $M_{a,b,c,d}$  direction for new BZs of assumed superstructures at 0.25 ML K coverage. The new zone boundaries by assumed K orderings in **a-d** are overlaid (dashed lines with corresponding colours). Absence of W-shape band at higher momentum above the assumed new zone boundaries, which can be induced by band folding, evidences that W-shaped band deformation is not due to the ordering of deposited K. **i,j**, Schematic drawings of conceivable scenarios for band deformation (hybridisation) by K deposition with assumed zone folded band (**i**) and upward convex band (**j**), respectively. Solid and dashed bands show the original and assumed bands, respectively. Both scenarios may exhibit band deformation, however, they should form the fragment of the original electron band at higher binding energy near BZ centre, which is absent in ARPES results (Fig. 4a).



**Extended Data Figure 8 | Band evolution induced by underlying lattice potential.** **a**, Crystal structure of the nine-slab model for the slab calculations. The vacuum layer with the thickness  $x$  along the  $c$ -axis is introduced in addition to the original interlayer space ( $d$ ). **b–e**, Calculated band structures depending on the vacuum thickness  $x$  of 20.0, 3.5, 1.0 and 0.0 Å, where the result of 0.0 Å is obtained by bulk calculation. Black arrows indicate the gradual shift of the surface electron band (blue) downward to the higher binding energy with a decrease in the vacuum thickness  $x$ . This exhibits that the surface electron state follows V-shape IAE band when it is strongly affected by underlying lattice.



**Extended Data Figure 9 | Resonant ARPES measurement after K deposition. a,b,** Band dispersions taken at off- (144 eV, **a**) and on-resonant (148 eV, **b**) condition of Gd  $4d$  core level after K deposition (deposition step #6). Lower panels are magnified images of the enclosed area by black dashed box in the upper panels. **c,** Normalised intensity (right) of the surface 2D electrons ( $I_{\text{Surface}}$ , blue) and trapped IAEs ( $I_{\text{IAE}}$ , brown), and their ratio (left, gray) as a function of photon energy.  $I_{\text{Surface}}$  and  $I_{\text{IAE}}$  are obtained by integrating the intensity of the shaded red area in lower panels and the exclusive area of red shade in upper panels of **a** and **b**, respectively.

**Extended Data Table 1 | Comparison of electron liquid on LHe and 2D electride.**

	<b>LHe</b>	<b>2D electride ([Gd<sub>2</sub>C]<sup>2+</sup>·2e<sup>-</sup>)</b>
Regime	Classical (non-degenerated)	Quantum (degenerated)
Electron density $n$ (cm <sup>-2</sup> )	~ 10 <sup>9</sup>	~ 10 <sup>14</sup>
Effective mass $m^*$ ( $m_e$ )	~ 1.0	~ 2.1
Fermi energy $E_F$ (meV)	~ 30	~ 250
Temperature $T$ (K)	~ 1	~ 10
Spin polarization	X	O